On the stability of medium gap corotating spiral Poiseuille flow

Alvaro Meseguer[a] and Francisco Marques[b]
Departament de Física Aplicada, Universitat Politécnica de Catalunya, C/ Jordi Girona 1-3, Modul B5, Barcelona 08034, Spain

(Received 11 April 2005; accepted 14 July 2005; published online 15 September 2005)

New features of the linear stability of the spiral Poiseuille flow for a wide range of inner and outer independent rotation speeds of the cylinders and imposed axial pressure gradient are investigated. The analysis is focused on the corotating situation and for a particular radius ratio $\eta=0.5$. Unexpected changes in the angle of the bifurcated spiral regimes are found for moderate values of the axial speed as the outer rotation is increased. In particular, tricritical points are detected, where modes associated with azimuthal wave numbers of opposite signs coexist at criticality. The present study is extended to high values of the axial speed of the flow and, to the authors' knowledge, the complete critical surface in the three-dimensional parameter space is obtained for the first time, providing new results on the behavior of the Tollmien-Schlichting instability. Increasing the rotation rate of the outer cylinder, the Tollmien-Schlichting instability is no longer dominant, resulting in a dramatic decrease in the critical axial Reynolds number. The sudden appearance of turning points in the critical curves recently obtained by other authors is also explained in terms of the geometry of the critical surface. © *2005 American Institute of Physics*. [DOI: 10.1063/1.2046708]

I. INTRODUCTION

The spiral Poiseuille problem deals with the behavior of an incompressible viscous fluid confined between two coaxial cylinders independently rotating around their common axis. In addition, the fluid is enforced to flow downstream by an imposed pressure gradient in the axial direction. The resulting steady spiral flow is a combination of a rotation due to the azimuthal Couette flow and an axial parabolic profile, due to the pressure gradient, also termed *spiral Poiseuille flow*.[1] Pressure-driven flows are of common usage in industry for many purposes such as cooling of rotating electrical machinery, purification of industrial waste water, or optical fiber fabrication techniques.[2,3] Beyond the practical applications of this kind of flows, there are many theoretical aspects that are of interest for the fluid dynamicist regarding the stability of the basic regime.

The stability of this flow has been studied numerically and experimentally by many authors.[4–9] A first comprehensive linear stability analysis was provided by the present authors[8] for medium gap, where the study covered a wide range of independent angular speeds of the cylinders as well as axial flow velocities. A recent work[9] has extended the analysis to much higher axial velocities, for four values of the ratio of the cylinders' angular velocities; they have established the connection between the Tollmien-Schlichting instability typical of Poiseuille flow with the centrifugal instability due to the rotation of the cylinders. In this study some of the results provided in our earlier studies[8] were shown to be inaccurate due to a lack of spectral resolution in the azimuthal direction when the outer rotation or the axial speeds are moderately high. Although our previous results were correct for all axial speeds and low or moderate outer rotation velocities, more accurate computations are required when centrifugal mechanisms become more important. The present work corrects our previous analysis[8] and presents a much wider exploration in parameter space, extending previous results,[8,9] revealing new interesting phenomena, and providing some insights regarding the competition between centrifugal and shear instability mechanisms.

The paper is structured as follows. The mathematical and numerical formulations of the stability of the problem are presented in Sec. II. A comprehensive study regarding the particular difficulties that arise when computing the critical values from the linearized Navier-Stokes equations is presented in Sec. III. The stability of the problem for low or moderate axial Reynolds numbers is revisited in Sec. IV. The main new result in this section is the existence of a curve on the critical surface where the axial speed and angle of the bifurcated spirals change sign, resulting in a drastic and unexpected change in the bifurcated solution features. The accuracy and reliability of the results have been carefully analyzed, making comparisons with earlier works[8] where the azimuthal resolution was insufficient and tricritical azimuthal modes of opposite signs were overlooked. Finally, Sec. V is focused on the stability of the flow for high values of the axial Reynolds number, where the Tollmien-Schlichting instability is found. The main new result in this section is the computation of the critical surface in the corotating regime for a wide range of outer rotation Reynolds numbers. In Sec. V A a comparison with previous results[9] is presented, with very good agreement; the geometry of the computed linear stability surface offers a nice explanation of the sudden appearance of turning points in the critical curves recently obtained by other authors[9] for fixed values of the ratio of the cylinders' angular velocities.

[a]Electronic mail: alvar@fa.upc.edu
[b]Electronic mail: marques@fa.upc.edu

II. STABILITY FORMULATION AND NUMERICAL METHODS

We consider an incompressible fluid of kinematic viscosity ν and density ϱ which is contained between two concentric rotating cylinders whose inner and outer radii and angular velocities are r_i^*, r_o^* and Ω_i, Ω_o, respectively. In addition, the fluid is driven by an imposed axial pressure gradient. The independent dimensionless parameters appearing in this problem are the radius ratio $\eta = r_i^*/r_o^*$, which fixes the geometry of the annulus, the Couette flow Reynolds numbers $Ri = dr_i^*\Omega_i/\nu$ and $Ro = dr_o^*\Omega_o/\nu$ of the rotating cylinders, where $d = r_o^* - r_i^*$ is the gap between the cylinders, and the axial Reynolds number $Re = \bar{w}d/\nu$, where $\bar{w}$ is the mean axial flow in the annulus and measures the imposed axial pressure gradient.

Henceforth, all variables will be rendered dimensionless using d, d^2/ν, and ν^2/d^2 as units for space, time, and reduced pressure ($p = p^*/\varrho$), respectively. The Navier-Stokes equation and the incompressibility condition for this scaling become

$$\partial_t \mathbf{v} + (\mathbf{v}\cdot\nabla)\mathbf{v} = -\nabla p + \Delta \mathbf{v}, \quad \nabla\cdot\mathbf{v} = 0. \tag{1}$$

Let $\mathbf{v} = (u, v, w)$, the physical components of the velocity field in cylindrical coordinates (r, θ, z). The boundary conditions for $\mathbf{v}$ are

$$v(r_i) = Ri, \quad v(r_o) = Ro, \tag{2}$$

where $r_i = r_i^*/d = \eta/(1-\eta)$, $r_o = r_o^*/d = 1/(1-\eta)$. The steady velocity field $\mathbf{v}_B$ (spiral Poiseuille flow), independent of the axial and azimuthal coordinates (θ, z), and satisfying (1) and (2) is

$$\mathbf{v}_B = (u_B, v_B, w_B) = [0, Ar + B/r, C\ln(r/r_o) + D(r^2 - r_o^2)], \tag{3}$$

where $A = (Ro - \eta Ri)/(1+\eta)$, $B = \eta(Ri - \eta Ro)/[(1-\eta)(1-\eta^2)]$, $C = 2(1-\eta^2)Re/[(1-\eta^2) + (1+\eta^2)\ln\eta]$, and $D = (1-\eta)(\ln\eta)C/(1+\eta)$. We will use throughout the paper (Ri, Ro, Re) as nondimensional parameters, keeping $\eta = 0.5$ fixed. Other nondimensional groups are used by other authors, such as the Poiseuille number $P = -(\partial p^*/\partial z)d^3/\varrho\nu^2$, the rotation rate ratio $\mu = \Omega_o/\Omega_i$, and the Taylor number. Different Taylor numbers can be found in literature, and we are going to use $Ta = d^2\Omega_i/\nu$, as defined in previous studies,[6,9] for comparison purposes. The relationship between the different nondimensional numbers is

$$P = \frac{8Re(1-\eta)^2\ln\eta}{1-\eta^2+(1+\eta^2)\ln\eta}, \quad \mathrm{Ta} = \frac{(1-\eta)Ri}{\eta}, \quad \mu = \frac{\eta Ro}{Ri}. \tag{4}$$

For $\eta = 0.5$ we obtain $P = 11.9063\,Re$, $Ta = Ri$, and $\mu = Ro/2Ri$.

The basic flow is perturbed by a small disturbance which is assumed to be periodic in the azimuthal and axial coordinates:

$$\mathbf{v}(r,\theta,z,t) = \mathbf{v}_B + \mathbf{u}(r)e^{i(n\theta+kz)+\lambda t}, \tag{5}$$

$$p(r,\theta,z,t) = p_B + q(r)e^{i(n\theta+kz)+\lambda t}, \tag{6}$$

where $\mathbf{v}_B = (0, v_B, w_B)$ is given by (3); the azimuthal wave number must be integer ($n \in \mathbb{Z}$), $k \in \mathbb{R}$, and $\lambda \in \mathbb{C}$. The perturbation of the velocity field is solenoidal and also satisfies homogeneous boundary conditions:

$$\mathbf{u}(r_i) = \mathbf{u}(r_o) = \mathbf{0}. \tag{7}$$

A formal substitution of the perturbed fields (5) and (6) in the Navier-Stokes equations (1) leads to the eigenvalue problem

$$\lambda\mathbf{u} = -\nabla q + \Delta\mathbf{u} - (\mathbf{v}_B\cdot\nabla)\mathbf{u} - (\mathbf{u}\cdot\nabla)\mathbf{v}_B, \tag{8}$$

where nonlinear terms have been neglected. The boundary value problem (7) and (8) is numerically discretized, making use of a solenoidal Petrov-Galerkin[10] spectral method already formulated and tested in the study of other spiral flows,[11] where the perturbation velocity is approximated via expansions of solenoidal fields built up from suitably modulated Chebyshev polynomials in the radial direction. Explicit expressions of the velocity fields used in the expansion are given in Meseguer and Marques.[11] For each (n,k) azimuthal-axial mode, the radial discretization over a Gauss-Lobatto mesh leads to a generalized eigenvalue problem,

$$\lambda\mathbb{G}(\eta,n,k)X = \mathbb{H}(Ri,Ro,Re,\eta,n,k)X, \tag{9}$$

where X contains the coefficients of the spectral approximation of the velocity field $\mathbf{u}$. Due to the solenoidal constraint, identically satisfied by X, the (n,k) Fourier subspace is two dimensional. Therefore, the matrices $\mathbb{G}$ and $\mathbb{H}$ resulting from the projection of the linearized Navier-Stokes operator are of size $(2M+1)\times(2M+1)$, where M is the number of trial spectral functions used in the radial discretization. The problem is then reduced to the computation of the spectrum of eigenvalues of (9) via any standard numerical linear algebra package such as LAPACK. The condition of criticality is obtained when the rightmost eigenvalue of the spectrum of (9) crosses the imaginary axis ($\Re\lambda = 0$). This condition must be imposed for each set of values of the parameters, resulting in an implicit dependence between the parameters of the perturbation $(n,k,\Im\lambda)$ and the set of Reynolds numbers (Ri,Ro,Re). The symmetries allow us to restrict the exploration to the cases $Re > 0$ and $Ri > 0$. Furthermore, since the Navier-Stokes equations are real, the complex conjugate of a perturbation (5) and (6) is also a solution, and we can change simultaneously the sign of n and k and the imaginary part of λ. Therefore, the exploration in the normal-mode analysis can be reduced to the case $k \geqslant 0$ and $n = 0, \pm 1, \pm 2, \ldots$. When axisymmetric modes $n = 0$ are dominant in the transition, the bifurcated pattern is the Taylor vortex flow, provided that $k \neq 0$. In addition, if the imaginary part of the rightmost eigenvalue, $\omega = \Im\lambda$, is not zero, these Taylor vortices will travel in the axial direction with a constant speed $c = \omega/k$. When n and k are nonzero, the eigenvector of the linear problem has the form of a spiral pattern. The wave numbers n and k, together with ω, fix the shape and speed of the spiral. The angle α of the spiral with a z-constant plane is given by $\tan\alpha = -n/(r_o k) = -(1-\eta)n/k$; the speed of the spiral in the axial direction (on a θ-constant line) is $c = -\omega/k$, and the precession frequency in the azimuthal direction is $\omega_{\mathrm{pr}} = -\omega/n$.

Let σ be the real part of the rightmost eigenvalue λ of the spectrum of (9). σ depends on the physical parameters and the axial and azimuthal wave numbers of the perturbation: $\sigma(Ri,Ro,Re,\eta,n,k)$. For fixed values of η, Ro, Re, and (n,k)-azimuthal-axial normal mode given, the inner Reynolds number $Ri^c(n,k)$ such that $\sigma=0$ is computed. The critical inner Reynolds number is given by $Ri^c=\min_{n,k}Ri^c(n,k)$, and the corresponding values of n and k are the critical azimuthal and axial wave numbers n^c and k^c which will dictate the geometrical shape of the critical eigenfunction. Furthermore, the imaginary part of the critical eigenvalue ω^c gives the angular frequency of the critical eigenfunction. The critical values Ri^c, n^c, k^c, and ω^c are implicit functions of the parameters η, Ro, and Re.

In order to visualize the flow corresponding to the critical modes, a helical streamfunction[8] will be used. Due to the periodicity (5) in (θ,z), the eigenvectors are functions of two coordinates only, r and $\zeta=n\theta+kz$. This allows the introduction of a helical streamfunction $\chi(r,\zeta)$ such that

$$u=-\frac{1}{r}\frac{\partial\chi}{\partial\zeta},\quad w=\frac{1}{kr}\left(\frac{\partial\chi}{\partial r}-nv\right). \tag{10}$$

The fluid particles move on χ=constant surfaces.

III. ON THE COMPUTATION OF CRITICAL VALUES

This section is focused on the multiple difficulties that may appear when computing the critical values Ri^c as a function of Re and Ro, or those of Re^c as a function of Ri and Ro. The *neutral stability curves* (NSCs) may exhibit multiple minima and disconnected regions of instability of arbitrary sizes and shapes.[8,9] This phenomenon is better understood when looking at the neutral stability surfaces on a three-dimensional projection. For example, Fig. 1(a) shows the $\sigma(Re,Ri,k)=0$ isosurface for $Ro=450$ and $n=-5$ within the range $(Re,Ri,k)\in[80,110]\times[100,900]\times[0,6]$. The keel shape of this surface is responsible for the multiplicity of critical points and islands of instability. Figure 1(b) shows the NSC cross sections of the neutral stability surface appearing in Fig. 1(a) for different values of Re. For $Re<78.72$, the NSC has a unique minimum, but when $Re=78.72$ a point of instability [black dot in Fig. 1(b)] appears at $(k^c,Ri^c)=(0.619,310.0)$, in coexistence with the no longer dominant critical value $(k^c,Ri^c)=(3.673,748.8)$ of the upper branch (white dot at the thick curve $Re=78.72$ in Fig. 1(b)). From that value of Re on, a dominant island of instability grows [the keel in Fig. 1(a)] and merges with the upper branch [curves $Re=80$, 90, 100, and 110 of Fig. 1(a)]. This is just an example of how difficult it can be to detect the instability region and to compute the minimum value of the NSC, even for a single azimuthal mode. This fact affects the exploration when varying Re since nothing is known in advance about the topological features of the NSC.

Another pathology that can be present in the structure of the NSC is the coexistence of two minima with clearly different axial and/or azimuthal wave numbers. This is observed in Fig. 2(a), where the NSC corresponding to the $n=-4$ and $n=-2$ modes for $Ri=0$ and $Ro=198.485$ have been plotted in a semilogarithmic scale. At the top right of Fig. 2(a) the NSC associated with the $n=-2$ mode consists of a parabolic boundary with a minimum at $(k^c,Re^c)=(1.47,1.013\times10^4)$. On the left, the NSC corresponding to the $n=-4$ mode has also been included, whose minimum lies close to the point $(k^c,Re^c)=(2.073\times10^{-2},1.010\times10^3)$, thus being the critical one. The corresponding values of k_c differ in two orders of magnitude, and the width of the instability region for the $n=-2$ mode is of order $O(\Delta k)\sim1$, whereas the NSC curve of the dominant mode $n=-4$ has a very narrow width of order $O(\Delta k)\sim10^{-3}$. In addition, very small variations of Ro may lead to large increments in (k^c,Ri^c). Figure

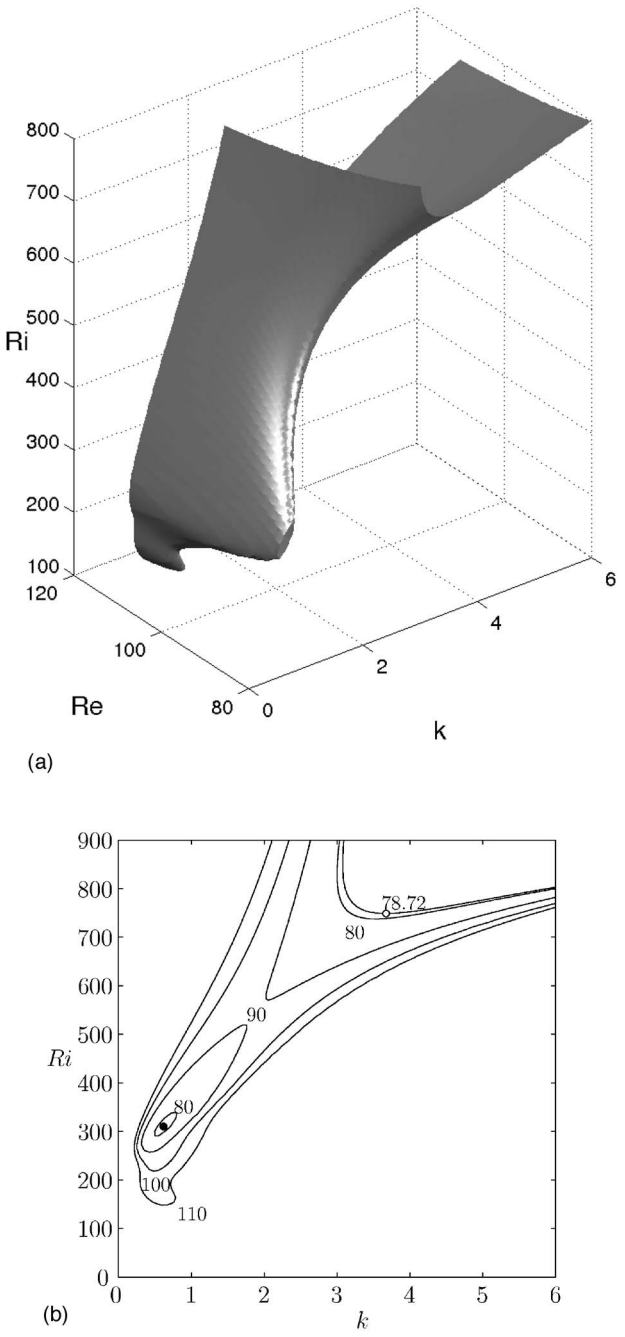

FIG. 1. (a) Neutral stability surface corresponding to the $n=-5$ azimuthal mode for $Ro=450$. (b) Neutral stability curves for $Re=80$, 90, 100, and 110 corresponding to sections of (a).

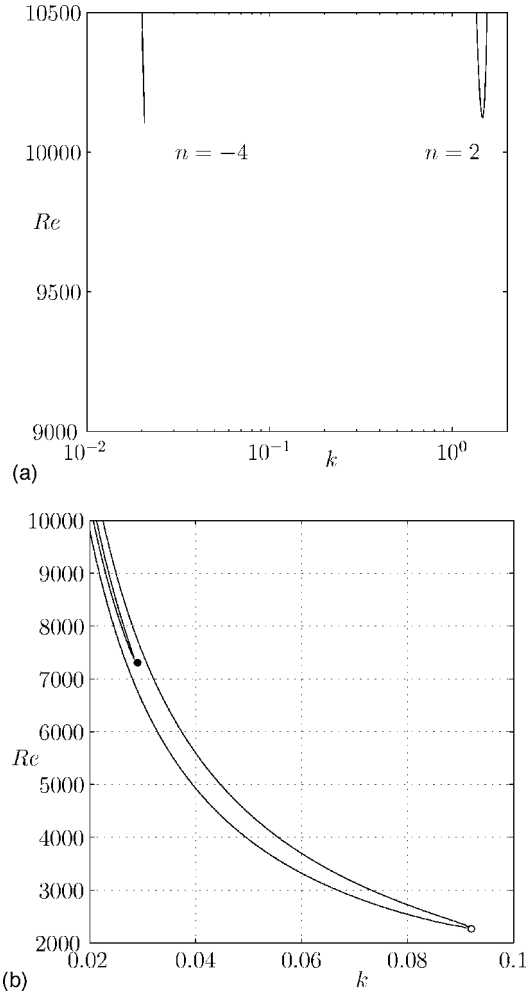

FIG. 2. (a) Neutral stability curves corresponding to $n=-4$ (bottom left) and $n=-2$ (top right) for $Ri=0$ and $Ro=198.485$. (b) Close-up of the curve corresponding to $n=-4$ in (a).

2(b) illustrates the rapid change of the topological structure of the NSC for $n=-4$. For $Ro=198.51$, the critical point [black dot in Fig. 2(b)] is located at $(k^c, Ri^c) = (0.029, 7307.1)$, whereas for Ro=199.02 the critical value has decreased drastically [white dot in Fig. 2(b)] to the point $(k^c, Ri^c) = (0.092, 2267.7)$; a change of 0.26% in Ro changes Ri^c by a factor of 3.2. Consequently, a fine grid in Ro needs to be used in the exploration, increasing the computational cost. Overall, the unexpected large variations of azimuthal and axial wave numbers, in combination with the strong gradients of the critical Reynolds numbers resulted in some errors in our previous study.[8]

A comprehensive exploration in the (k, Re) plane within the interval $(k, Re) \in [0, 10] \times [0, 1.5 \times 10^4]$ on a regular equispaced grid would require a huge amount of evaluations of the spectrum of eigenvalues of (9) in order to detect the instability tongue shown in Fig. 2(b) or the instability island for $Re=80$ shown in Fig. 1(b). For this reason, it is necessary to work with a *self-adaptive* grid width, at least in the k variable. The present computations have been carried out using an evaluation method in a nonuniform grid k_j with increments $\Delta k = k_{j+1} - k_j$ which are suitably adapted at every point of the geometry of the function σ. For this purpose, a

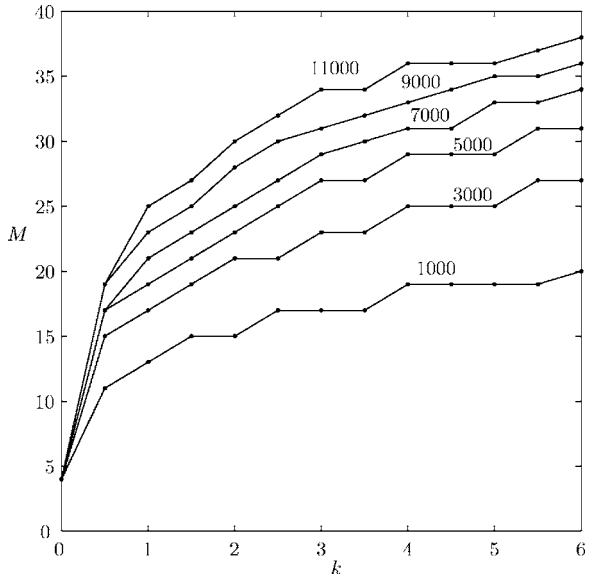

FIG. 3. Minimum number of radial spectral modes M required for accuracy as a function of the axial Reynolds number Re within the range $Re \in [1 \times 10^3, 1.1 \times 10^4]$, and the axial wave number k, for $Ri=0$, $Ro=0$, and $n=5$.

local evaluation of the first derivative $\partial_k \sigma$ provides some insight on the behavior of the real part of the rightmost eigenvalue of (9). It is clear, from Fig. 2(b), that such a narrow region of instability is directly related to strong variations of $\sigma(k)$, for Re fixed. Wherever the algorithm detected high values of $\partial_k \sigma$, the Δk increments were automatically decreased to the required resolution. Once the algorithm detected a change of sign, a secant method was applied to converge to the desired critical minimum.

The reliability of the computed critical values lies on the radial resolution used to approximate the spectrum of eigenvalues of (9). It is a common practice to increase the number of radial modes M or collocation points as long as any of the Reynolds numbers is increased. The accuracy of the eigenvalues obtained might also be affected when increasing the axial or azimuthal wave numbers if there is no automatic

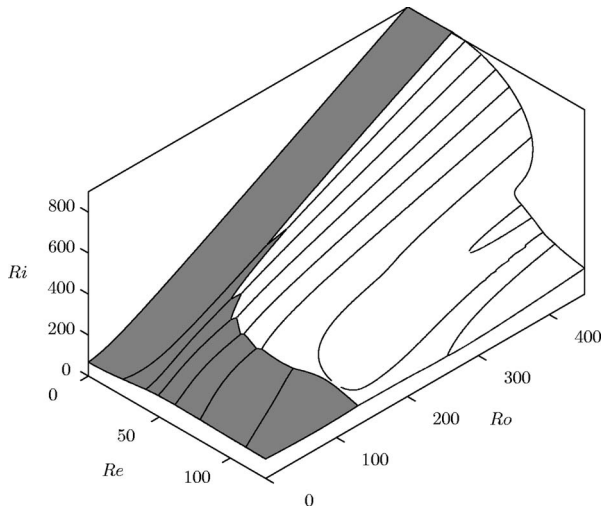

FIG. 4. Critical surface $Ri^c(Re, Ro)$. The shaded region corresponds to positive or zero azimuthal wave numbers.

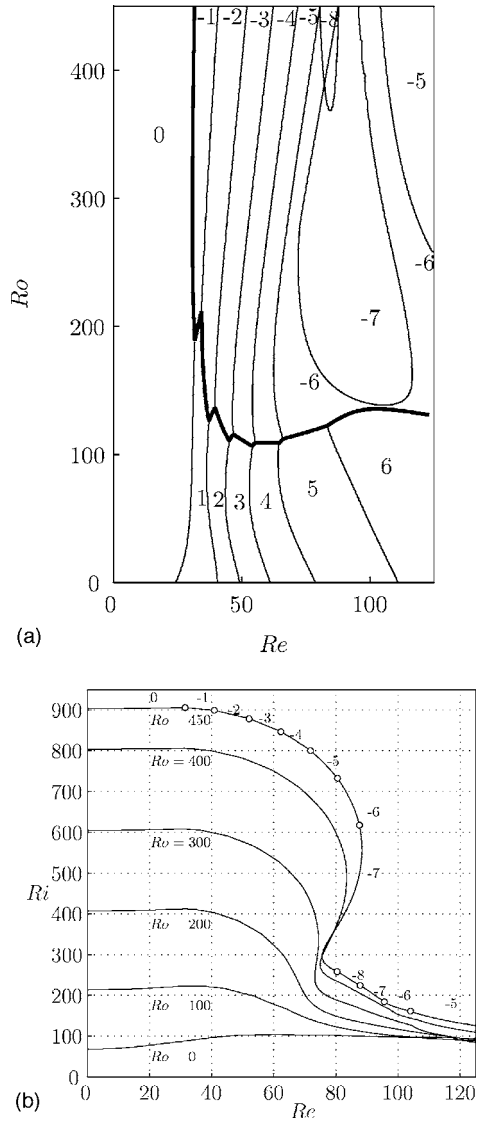

FIG. 5. (a) Projection of the critical surface boundary curves (Fig. 4) on the (Re,Ro) plane. (b) Ro-constant cross sections of the critical surface.

control of the radial order of approximation. As an example, Fig. 3 plots the required minimum of radial modes in order to compute the rightmost eigenvalue of (9) with a relative error $\varepsilon_r=\|(\sigma^M_{\max}-\sigma^{M_0}_{\max})/\sigma^{M_0}_{\max}\|$ less than 10^{-3}, where $\sigma^{M_0}_{\max}$ is an "exact" or reference value obtained with $M_0=64$. The analysis in Fig. 3 corresponds to the particular case $Ri=Ro=0$ (cylinders at rest) and azimuthal wave number $n=5$. Increasing n, Ri, or Ro requires more radial modes. The computations presented in this work have been done monitoring the value of M so that the rightmost eigenvalues computed at any point of the parameter space are converged to four significant digits.

IV. LINEAR STABILITY RESULTS FOR MODERATE *Re*

In this section, the exploration covers the corotation region $(RiRo>0)$ within the range $(Re,Ro,n,k)\in[0,125]\times[0,450]\times[-10,10]\times[0,25]$, for $\eta=0.5$. For each pair of values (Re,Ro), the critical values Ri^c, n^c, k^c, and ω^c have been computed.

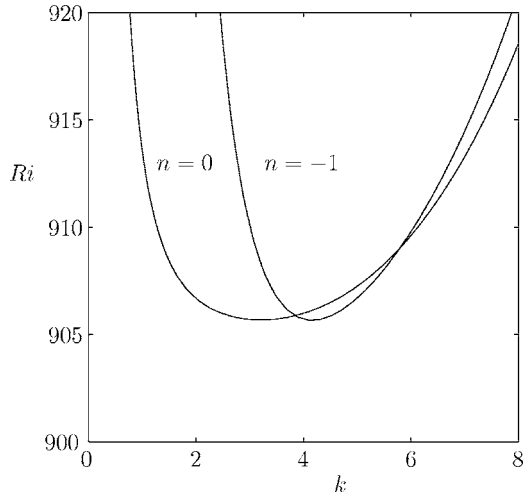

FIG. 6. Neutral stability curves of azimuthal modes $n=0$ and $n=-1$ for $Re=31.5$.

The critical surface $Ri^c=Ri^c(Re,Ro)$ has been plotted in Fig. 4. This critical surface was previously computed,[8] but part of the results were incorrect, as was pointed out in a recent similar study.[9] The curves on the critical surface in Fig. 4 correspond to changes in the azimuthal wave number n. In these bicritical curves, two eigenvalues with different n become simultaneously unstable. A projection of these curves on the (Re,Ro) plane, including the values of n, is plotted in Fig. 5(a). On many of these curves the change in n is $\Delta n=\pm 1$, but there is a curve [the thick line in Fig. 5(a)] where n changes sign, resulting in variations of n as large as $\Delta n=12$ units. These large increments in the azimuthal wave number were overlooked by the exploring algorithm used in the past in our earlier work.[8] Only the region on the critical surface where $n\geqslant 0$ was correctly computed, and it has been represented by a shaded region in Fig. 4. This large change in n is one of the several difficulties mentioned in Sec. III that make the computation of the critical surfaces in multiparameter problems so difficult. Although the qualitative shape of the stability surface is the same as the one that appeared in our studies in the past,[8] the critical parameters, such as the angle of the spirals α or their propagation speed c, are considerably different above and below the thick curve represented in Fig. 5(a) due to the change of sign of the azimuthal wave number n.

In Fig. 5(b), six cross sections of the critical surface have been plotted for quantitative analysis. The transition points between different azimuthal wave numbers have been included in the $Ro=450$ curve in order to compare with other studies;[9] a very good agreement is observed between both computations. The only difference is the location of the transition point between the $n=0$ and $n=-1$ modes,[9] where this transition seems to occur for $Re\sim 38.2$, although in the present computation this transition takes place for $Re=31.45$ (a 20% change), as can be observed from the neutral stability curves plotted in Fig. 6. The authors believe that there could be just a graphical, but not numerical, mistake in Fig. 6 of Ref. 9 when marking the transition with a transversal slash at the incorrect location.

TABLE I. Critical values at the tricritical points shown in Fig. 5(a).

n	Re	Ro	Ri^c	k^c	ω^c	c^c
	P	μ				
0				3.206	−118.9	37.08
−1	31.61	188.3	390.1	3.383	26.18	−7.740
1	376.4	0.2414		4.541	−382.0	84.11
−1				3.298	35.43	−10.74
1	34.29	212.0	434.9	4.575	−425.4	92.97
−2	408.2	0.2438		4.041	159.9	−39.58
1				4.011	−317.4	79.13
−2	37.15	126.1	270.8	3.494	49.73	−14.23
2	442.4	0.2329		4.868	−517.5	106.3
−2				3.368	60.04	−17.83
2	39.51	137.0	288.1	4.807	−550.7	114.5
−3	470.4	0.2378		3.881	136.6	−35.19
2				4.171	−483.1	115.8
−3	45.03	110.7	234.5	3.381	81.52	−24.11
3	536.2	0.2360		4.966	−670.7	135.1
−3				3.269	90.02	−27.54
3	46.59	115.9	240.1	4.872	−687.1	141.0
−4	554.7	0.2413		3.712	149.7	−40.32
3				3.961	−617.4	155.9
−4	54.11	106.5	207.7	3.062	124.1	−40.51
4	644.2	0.2563		4.747	−800.0	168.5
−4				2.972	130.9	−44.05
4	55.13	109.3	208.6	4.641	−803.5	173.1
−5	656.3	0.2620		3.374	181.6	−53.84
4				3.421	−697.4	203.8
−5	64.29	108.2	176.0	2.553	181.1	−70.93
5	765.5	0.3072		4.115	−866.4	210.5
−5				2.377	194.9	−82.03
5	66.09	112.2	172.7	3.847	−851.7	221.4
−6	786.8	0.3248		2.723	241.2	−88.56
5				2.067	−656.4	317.6
−6	83.23	122.3	126.0	1.578	281.5	−178.4
6	990.9	0.4854		2.509	−793.2	316.2

When the outer cylinder is at rest ($Ro=0$), axisymmetric perturbations are dominant for $Re \lesssim 24.2$. As long as Ro is increased, the threshold value for dominance of axisymmetric disturbances stagnates at nearly $Re \sim 31.5$. Nevertheless, the transition from axisymmetric to nonaxisymmetric azimuthal modes depends on the value of Ro. For instance, if $Ro < 189$, the transition is from $n^c=0$ to $n^c=1$. For $Ro > 189$, the dominant mode is no longer $n^c=1$ but $n^c=-1$, and this unexpected change was not detected in our previous computations[8] due to a lack of azimuthal resolution in that region. This abrupt change in the angular dependence of the critical perturbation leads to a transition to secondary spiral regimes with opposite angle and speed. The thick curve in Fig. 5(a) separates positive (or zero) from negative nonaxisymmetric modes. This curve is continuous, and the discontinuities in slope are due to the fact that n is an integer. Along this curve, tricritical points of coexistence of different spiral regimes have been computed accurately. The coordinates of these points and their associated transition values have been enlisted in Table I; the Poiseuille number P and the rotation rate ratio μ have also been included in the table. For low values of Re the tricritical points have nearly the same rotation rate $\mu=\Omega_o/\Omega_i \sim 0.24$, but this property disappears when increasing the axial speed of the basic flow. Above and below the thick line in Fig. 5(a), the bifurcated patterns are remarkably different. The spirals appearing below the frontier have a negative angle α and travel downstream with an axial speed c close to the Poiseuille mean speed, whereas above the bicritical curve both features, angle and axial speed, change sign.

In order to visualize the flow, we have used the helical streamfunction χ introduced in (10). The three spiral regimes corresponding to the $n=\pm 1$, 2 tricritical point have been visualized in Fig. 7. Contours of χ have been plotted in the (r,z) plane corresponding to $\theta=0$ in order to visualize the inner structure of the eigenmode. Three-dimensional views of two convenient isosurfaces $\chi=\pm$constant have also been included; dark/light isosurfaces correspond to negative/

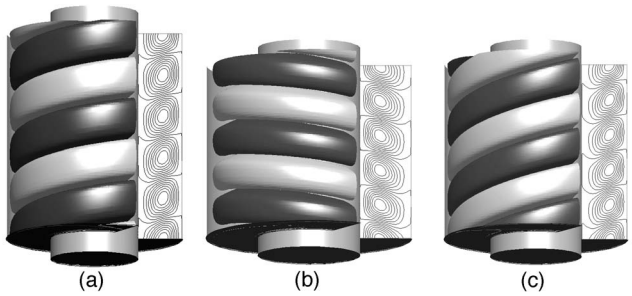

FIG. 7. Eigenfunctions of Table I corresponding to the tricritical point at the coordinates $(Re,Ro,Ri)=(34.29,212.0,434.9)$. From left to right, (a) $n=-1$, (b) $n=1$, and (c) $n=-2$ for $z\in[-5\pi/2k^c,-5\pi/2k^c]$, where k^c is the associated critical axial wave number with each mode.

positive values, respectively. For each azimuthal mode, two and a half axial wavelengths have been represented preserving the radial-axial scale for quantitave comparisons. The plotted spirals differ not only in their angle, axial speed, or periodicity, but also in the radial structure of the mode. Negative modes $n=-1,-2$ [Figs. 7(a) and 7(c)] tend to be clustered near the outer wall, whereas the positive mode $n=1$ (Fig. 7(b)) is concentrated near the inner cylinder.

V. LINEAR STABILITY ANALYSIS FOR HIGH *Re*

The present study has extended the exploration to higher values of the axial Reynolds number. First of all, we computed the critical axial Reynolds number for the particular case when both cylinders are at rest, the so-called Tollmien-Schlichting instability, already obtained by many authors.[9,12,13] In this particular case, for $\eta=0.5$ the modes with $n=\pm2$ are the first modes that become unstable in the precipitous fall at $Re^c=10\,359.2$ for $k^c=1.478\,25$, in very good agreement with $(Re^c,k^c)=(10\,359,1.479)$, obtained in a recent analysis.[9] In Table II, the critical values have been tabulated as a function of the order M of radial approximation; in order to obtain six significative digits, at least $M=38$ radial modes are required. These values confirm the necessity of increasing the radial resolution when the axial Reynolds number is particularly high.

The range covered by the present exploration is $(Ro,Re)\in[0,450.0]\times[0,2.0\times10^4]$, with $-10\leqslant n\leqslant10$ and $0\leqslant k\leqslant25.0$. Figure 8 shows a view of the complete linear stability surface of the corotating spiral Poiseuille flow,

TABLE II. Convergence of critical values Re^c and k^c as a function of the spectral order M for the critical Tollmien-Schlichting $n=\pm2$-mode ($Ri=Ro=0$).

M	Re^c	k^c
26	10 858.19	1.47 030
30	10 392.89	1.47 916
34	10 359.05	1.47 857
38	10 359.23	1.47 828
42	10 359.25	1.47 825
46	10 359.24	1.47 825

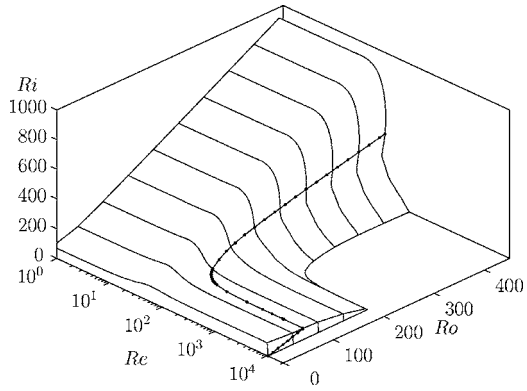

FIG. 8. Extended computation of the critical surface $Ri^c=Ri^c(Re,Ro)$ for $Ro\in[0,450]$. The dotted line on the surface corresponds to the particular case $\mu=0.5$.

where a logarithmic scale has been used in the *Re* axis (from 1 to 2.0×10^4). To the authors' knowledge, this complete surface within the corotating regime has never been computed before. On this surface the curve corresponding to the particular case $\mu=0.5$ has been plotted, and it will be studied in detail in Sec. V A. The three-dimensional view makes clear the presence of a turning point in some μ-constant curves, such as $\mu=0.5$ and the singular limit $\mu\to\infty$, i.e., the

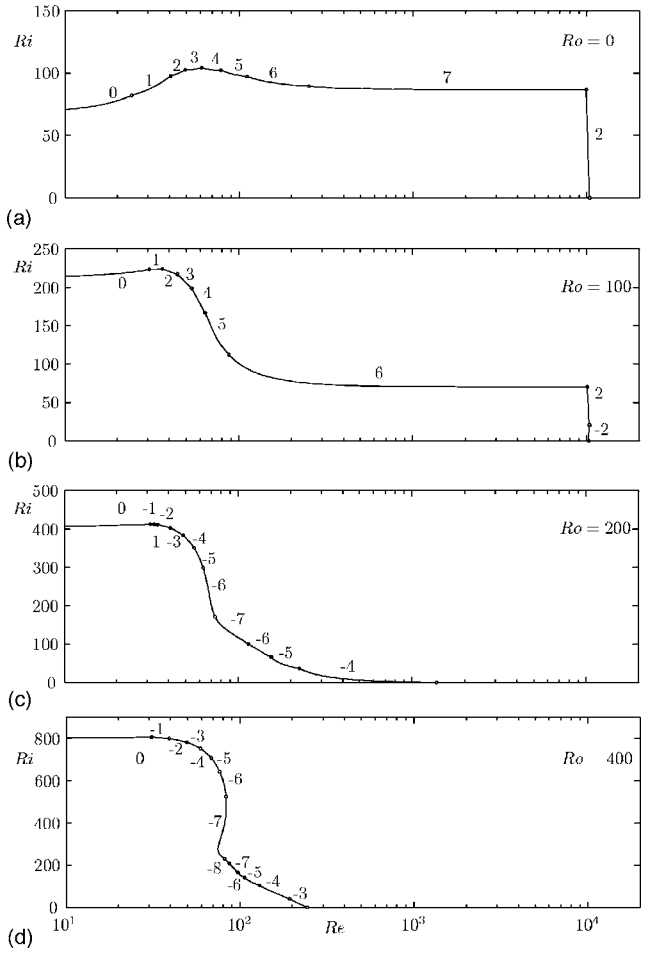

FIG. 9. Critical curves $Ri^c(Re)$ for different constant values of Ro; only four cases are included for clear visualization.

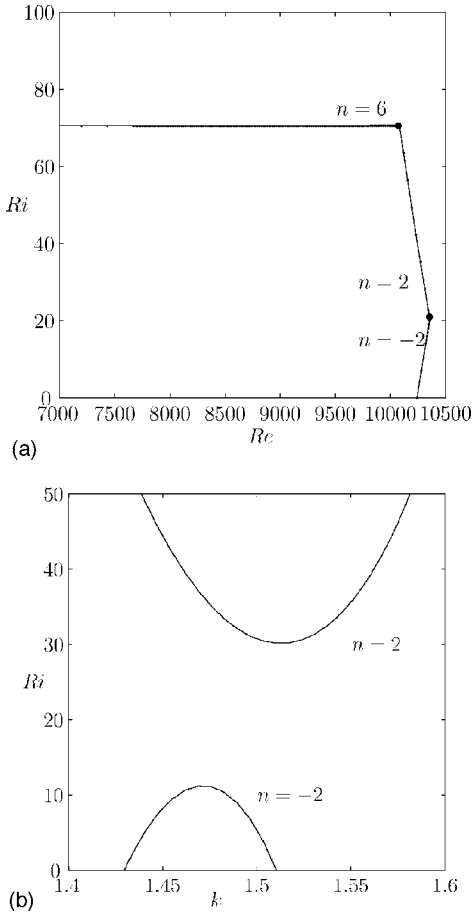

FIG. 10. (a) Details of the critical curve $Ro=100$ near the Tollmien-Schlichting instability region. (b) Neutral stability curves corresponding to the azimuthal modes $n=-2$ and $n=2$ for $Re=10300$ and $Ro=100$.

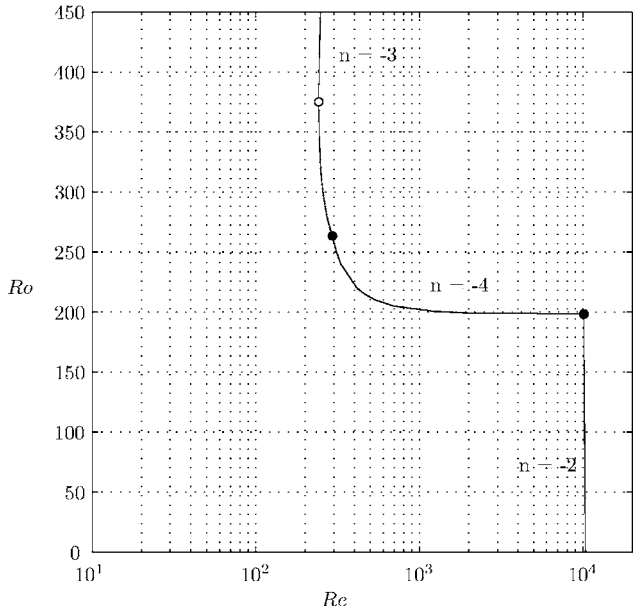

FIG. 11. Stability boundary on the $Ri=0$ plane.

intersection of the surface with the $Ri=0$ plane. This phenomenon, directly associated with the effects of the outer rotation Ro of the cylinder, will be analyzed later in Sec. V A.

The three-dimensional view in Fig. 8 shows a region of the (Re,Ro) plane where the critical inner Reynolds number is almost uniform. This *plateau* region is clearly visible for axial Reynolds numbers within the range $Re\in[10^3,10^4]$ and for low or moderate outer rotation Reynolds number $Ro\in[0,100]$. The critical surface exhibits a drastic fall for $Re\sim10^4$ due to the sudden dominance of the Tollmien-Schlichting instability. This feature disappears when increasing Ro. For $Ro>150$, the plateau starts to decrease its height gradually in the interval $Ro\in[150,200]$, and finally merges with the $Ri=0$ plane for an almost constant value $Ro=198.48$.

Figure 9 displays the most relevant features at high Re of the stability surface for different values of the outer rotation Reynolds number Ro. The curves associated to $Ro=0$ and $Ro=100$ share some qualitative features, although some differences must be pointed out. In both curves, the inner critical Reynolds number Ri^c stagnates at an asymptotic value before the Tollmien-Schlichting instability takes place. For $Ro=0$, within the interval $400<Re<Re_0^*=9915.6$, the inner rotation Reynolds number attains a critical value of $Ri_0^c=86.882$, thus revealing a near independence of the stability of the basic flow with respect to the axial shear [Fig. 9(a)]. The dominant azimuthal mode in this almost asymptotic regime is $n^c=7$, in agreement with previous computations[9] for $\mu=0$. At $Re=Re_0^*$, the $n^c=2$ azimuthal mode becomes dominant, leading to a drastic fall of Ri^c within the range $Re_0^*<Re<10\,359.2$, where the Tollmien-Schlichting instability appears.

The geometrical features of the critical surface suffer small, but relevant, changes when Ro is increased. For $Ro=100$ and $850<Re<Re_{100}^*=10071$, the value of the critical inner rotation decreases to $Ri_{100}^c=70.549$, and the dominant azimuthal wave number decreases as well to $n^c=6$ [Fig. 9(b)]. Above Re_{100}^*, $n^c=2$ becomes the dominant azimuthal mode, starting a drastic fall of Ri^c. In contrast with the $Ro=0$ curve, $n^c=-2$ is the first mode that becomes unstable in the precipitous fall at $(Re,Ri)=(10\,354,20.5)$, where the critical boundary exhibits a turning point, shown in Fig. 10(a), thus decreasing the axial Reynolds number in the Tollmien-Schlichting region to $Re=10241$. This phenomenon can be understood when looking at the NSC corresponding to the modes $n=\pm2$ in Fig. 10(b) for $Ro=100$ and $Re=10\,300$. According to the location of the maximum and minimum of the two azimuthal modes shown in Fig. 10(b), there is a range of values of inner rotation Reynolds numbers within which the basic flow remains stable. As a result, the *precipitous fall* is multivalued (at least when $Ro\neq0$) near the Tollmien-Schlichting region. The competition between $n=-2$ and $n=2$ for low rotations is expected, since the rotational symmetry is broken by the presence of very small azimuthal speeds, relative to the axial velocity in that region.

The critical surface shown in Fig. 8 exhibits a flat plateau followed by a precipitous fall for a moderate outer rotation Reynolds number Ro. These features disappear above a threshold value of $Ro=198.48$. The stability boundary for $Ri=0$ depicted in Fig. 11 for $Ri=0$ clearly shows the change

TABLE III. Critical values corresponding to the transition boundary of Fig. 11 for $Ri=0$.

Ro	Re^c	n^c	k^c	ω^c	c^c
0	10 359	±2	1.478	−6190.6	4188.5
50.0	10 300	−2	1.476	−6118.8	4145.5
100.0	10 241	−2	1.473	−6045.8	4104.4
150.0	10 183	−2	1.469	−5971.8	4065.2
198.48^-	10 128	−2	1.466	−5893.6	4020.2
198.48^+	10 128	−4	0.021	144.8	−6896.7
200.0	1 379.3	−4	0.152	136.0	−894.8
250.0	310.31	−4	0.659	232.9	−353.4
300.0	256.58	−3	0.605	240.8	−398.0
350.0	243.44	−3	0.637	305.7	−479.9
375.1	242.40	−3	0.643	339.6	−528.2
400.0	242.86	−3	0.645	369.7	−573.0
450.0	247.38	−3	0.646	432.8	−670.0

of behavior taking place at $Ro=198.48$. The Tollmien-Schlichting $n^c=-2$ instability is dominant within the interval $Ro\in[0,198.48^-]$. For $Ro>198.48$, the outer rotation becomes the dominant mechanism at the transition point $(Re,Ro)=(10\,128,198.48)$ with $n^c=-4$. Within the range $Ro\in[198.48^+,263.4]$, the axial critical Reynolds number decreases nearly by two orders of magnitude. This feature was already pointed out in Sec. III as one of the unexpected pathologies of the NSC shown in Fig. 2(b). After this remarkable fall, the outer rotation seems to stabilize the basic flow, as reflected in the turning point of the transition boundary, located at $(Re,Ro)=(242.4,375.1)$ on the plane $Ri=0$ in Fig. 8, above which increasing the outer rotation results in a small increase in the stability of the base flow. Overall, Table III contains the most relevant critical values of the boundary plotted in Fig. 11.

Figure 12 shows the critical axial wave number k^c as a function of Re for the same values of Ro as in Fig. 9. An interesting feature is that the axial periodicity of the secondary regimes is always bounded within the explored domain, with a maximum value of k close to 5.0. For low or moderate rotations, the axial wave number suffers a remarkable change when approaching the Tollmien-Schlichting instability. For $Ro=0$, the critical axial wave number decreases down to $k^-=0.042$ when increasing Re (the plateau with $n=7$ in Fig. 9(a) just before experiencing an increase by a factor of 35 up to $k^+=1.4820$, when the $n=2$ becomes dominant, reflected in the isolated dots on the right of Fig. 12(a). The same qualitative behavior is observed for $Ro<198.48$ [Fig. 9(b)], just before the dominance of the outer rotation instability mechanism over the axial shear. The decrease in k can be seen in Fig. 12(c) and 12(d) for $Ro=200$ and $Ro=400$, where the huge jump in k for large Re is absent.

Figure 13 shows the normalized axial speed c/Re as a function of Re for the same values of Ro as in Fig. 9. The dimensional axial speed is $c^*=c\nu/d=(c/Re)\bar{w}$, where $\bar{w}$ is the mean axial flow of the basic flow introduced at the beginning of Sec. II. Therefore c/Re measures the axial speed of the critical modes in units of $\bar{w}$. If we had used $d/\bar{w}$ as the time scale instead of the viscous time d^2/ν (as in Refs. 6 and 9, we would have obtained c directly in $\bar{w}$ units. Therefore, the relationship between the c_{crit} axial speed appearing in Ref. 9 and our c is $c_{\mathrm{crit}}=c/Re$. When the outer cylinder is at rest or rotating with low speed (curves $Ro=0$ and 100 in Fig. 13), the spirals have negative angles ($\alpha<0$) and move downstream with the basic axial flow with speeds slightly higher than the Poiseuille profile. This behavior no longer

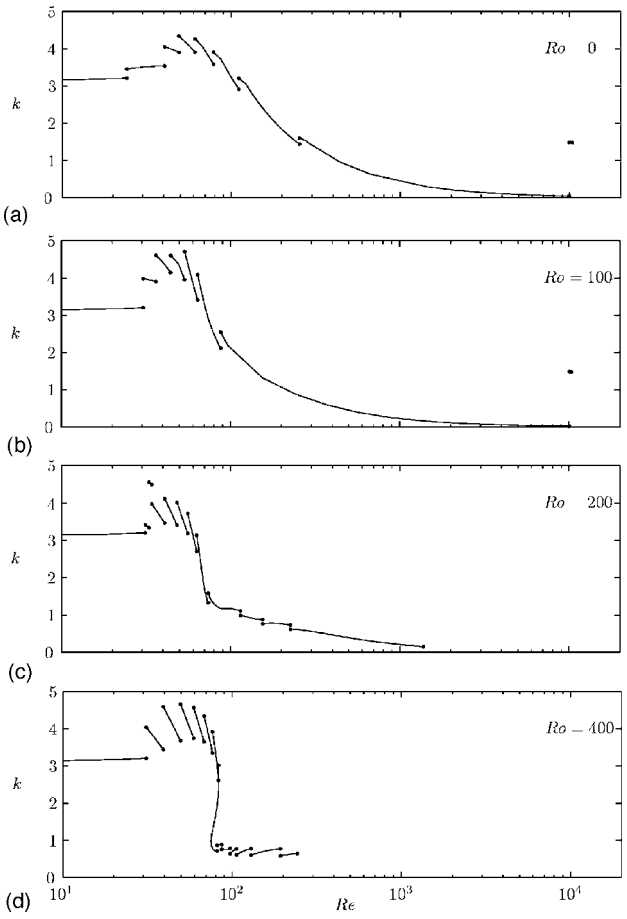

FIG. 12. Critical axial wave number k^c as a function of Re for the same values of Ro shown in Fig. 9.

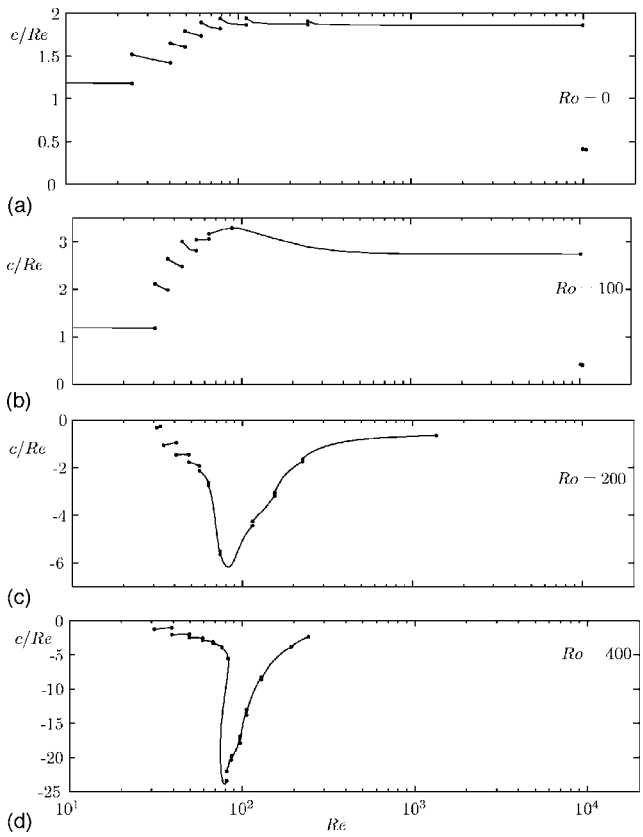

FIG. 13. Normalized axial speed c/Re of the secondary patterns for the same values shown in Fig. 9 and 12.

persists for higher outer rotations (curves $Ro=200$ to 450 in 13), and the spirals have the same helical orientation as the basic flow ($\alpha>0$) but move upstream with speeds much higher than in the low Ro case.

Three different eigenmodes have been plotted in Fig. 14, showing the essential features of the secondary regimes for high values of Re. Figure 14(a) shows an $n=6$ mode corresponding to the plateau in Fig. 9(b) for $Re=1066$, $Ro=100$, and $Ri^c=70.78$. The angle of the spirals is $\alpha=-86°$ and $\alpha\to-90°$ when Re increases up to the Tollmien-Schlichting instability boundary shown in Fig. 10(a). Figure 14(b) shows an $n=-4$ mode corresponding to the stability boundary in Fig. 11 for $Re=1000$, $Ro=201.44$, and $Ri=0$. The angle of the spirals is $\alpha=84°$ and $\alpha\to90°$ when Re approaches the precipitous fall at $Re=10\,128$. Figures 10(a) and 10(b) are examples of the change of sign of n that has been described in Sec. IV. In fact, the thick line in Fig. 5(a) extends to high Re keeping Ro almost constant up to the Tollmien-Schlichting instability boundary. Figure 14(c) shows the $n=-2$ Tollmien-Schlichting mode at criticality for $Re=10359$ and $Ri=Ro=0$, corresponding to the last point in Fig. 11. In fact, for $Ri=Ro=0$ both modes $n=\pm2$ bifurcates simultaneously, and the eigenfunctions for the $n=2$ mode is the same as for $n=-2$ but reflected on the plane $\theta=0$. In all three cases shown in Fig. 14, the axial-radial scale has been preserved. Nevertheless, Figs. 14(a) and 14(b) only show half a period of the eigenmodes, due to their streamwise extent determined by their axial wavelength ($\lambda_6=2\pi/k^c\sim30$ and $\lambda_{-4}=2\pi/k^c\sim30$).

FIG. 14. Spiral eigenmodes for high values of Re.

A. Comparisons with previous computations ($\mu=0.5$)

Cotrell and Pearlstein[9] provided the complete stability boundary for a particular set of rotation-rate ratios $\mu=-0.5$, 0, 0.2, 0.5, where the parametrization was based on variations of the *Taylor* number Ta. The (μ,Ta) parametrization is related to our variables (Ri,Ro) according to relations (4): $Ta=Ri$, $\mu=\eta Ro/Ri=Ro/2Ri$. Therefore, the critical curves appearing in Ref. 9 correspond to different intersections of the critical surfaces shown in Figs. 4 or 8 with the planes $Ri=\eta Ro/\mu$. As stated before, the (μ,Ta) parametrization may lead to complications when exploring the stability. In particular, this parametrization is singular when the inner cylinder is at rest $Ri=0$ and the outer is not, i.e., $\mu\to\infty$. A clear example of the complexity of the (μ,Ta) parametrization is reflected in Fig. 5 of Ref. 9, where the critical boundaries for $\mu=0$ and $\mu=0.2$ are qualitatively similar but the $\mu=0.5$ case exhibits a turning point absent in the other cases. This behavior can be clearly understood looking at the geometry of the critical surface in Fig. 8. For $Re\lesssim50$ and for $Ro>50$ the critical surface becomes asymptotic to the plane $\mu=\eta^2=0.25$, corresponding to the Rayleigh stability criterion for the Taylor-Couette flow.[14] For $\mu<\eta^2$ the μ-constant planes cut the asymptotic plane, while for $\mu<\eta^2$ they do not cut the asymptotic plane, resulting in the latter case in a critical curve with a turning point, as shown in Fig. 8 for $\mu=0.5$. For $\mu\sim\eta^2$, the μ-constant planes are almost tangent to the asymptotic plane, and very small variations of μ result in extremely large changes in the critical parameters.

By using relations (4), the numerical algorithm used in this study can be suitably modified in order to recover Cotrell and Pearlstein's results for the particular case $\mu=0.5$. This computation has also been particularly useful in order to validate the azimuthal resolution of the spectral method. In Fig. 15, the critical Taylor number Ta^c has been plotted as a function of the axial Reynolds number Re, following Fig. 2(a) of Ref. 9. The three-dimensional projection

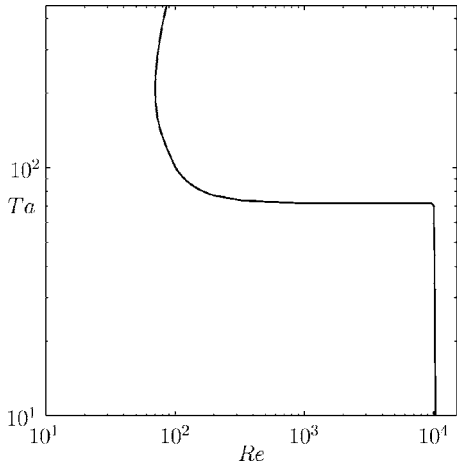

FIG. 15. Critical Taylor number Ta^c as a function of the axial Reynolds number Re^c for $\mu=0.5$.

of this curve has been represented also in Fig. 8 for clarity. The most relevant critical values corresponding to Fig. 15 have been included in Table IV. For $Ta=0$, the critical Reynolds number corresponds to the Tollmien-Schlichting instability mentioned before attained at $Re^c=10\,359.2$, which is in a very good agreement with the computations provided in Ref. 9. The critical Reynolds number Re does not suffer a remarkable change for $Ta<70.0$. Within the range $70.0 \leqslant Ta \leqslant 77.30$ the critical Reynolds number exhibits a fall nearly by two orders of magnitude. For higher values of Ta, the centrifugal mechanism has a stabilizing effect over the basic flow. This fact is clearly reflected in the turning point that the axial Reynolds number presents at the coordinates $(Ta^c, Re^c)=(200.0, 70.2)$ after which the critical axial Reynolds number grows monotonically when increasing Ta from that value.

VI. CONCLUSIONS

A comprehensive linear stability analysis of a spiral Poiseuille flow has been provided for a medium gap geometry ($\eta=0.5$) and with independently corotating cylinders. The detailed exploration for low axial speeds and the increased resolution in the azimuthal direction with respect to previous studies have revealed new and unexpected bifurcation phenomena. The presence of a curve on the critical surface separating positive and negative azimuthal wave numbers results in a drastic and unexpected change in the axial speed and angle of the bifurcated spirals. On this curve, tricritical points where three different spiral modes bifurcate simultaneously have been accurately computed. Complex nonlinear dynamics due to mode interaction is likely to be expected near this curve, deserving further numerical and experimental studies.

The exploration has been enhanced to high axial Reynolds numbers, computing the critical surface for the first time and providing new results on the behavior of the Tollmien-Schlichting instability. In particular, close to an outer rotation Reynolds number of $Ro \sim 198.48$, a drastic change takes place in the instability mechanism: the Tollmien-Schlichting instability is no longer dominant and the large plateau characteristic of small Ro values disappears, resulting in a dramatic decrease in the critical axial Reynolds number Re. This phenomenon is explained by studying the critical values when the inner cylinder is at rest.

Finally, the geometry of the computed linear stability surface offers a nice explanation of the presence of turning points in the critical curves recently obtained by other authors[9] for fixed values of the ratio of the cylinder's angular velocities μ. The sudden appearance of these turning points is due to a tangency with the critical surface when a parametrization based on (Ta, μ) is used. The critical surface becomes asymptotic to the plane $\mu=\eta^2=0.25$, corresponding to the Rayleigh stability criterion for the Taylor-Couette flow, and very small variations of $\mu \sim \eta^2$ result in extremely large changes in the critical parameters, including the sudden appearance of turning points.

TABLE IV. Critical values for $\mu=0.5$.

Ta^c	Re^c	k^c	n^c
0.00	10 359.2	1.478	2
70.00	10 056.8	1.486	2
71.74	9 706.2	0.056	6
77.30	200.0	1.135	6
180.00	70.8	1.680	−6
200.00	70.2	1.692	−6
220.00	70.3	1.696	−6

ACKNOWLEDGMENT

This work was supported by the Spanish Ministry of Science and Technology, Grant No. FIS2004-01336.

[1] D. D. Joseph, *Stability of Fluid Motions I and II*, in Springer Tracts in Natural Philosophy Vol. 27 (Springer, Berlin, 1976).
[2] D. F. Ollis, E. Pelizzetti, and N. Serpone, "Photocatalyzed destruction of water contaminants," Environ. Sci. Technol. **25**, 1523 (1991).
[3] K. Chida, S. Sakaguchi, M. Wagatsuma, and T. Kimura, "High-speed coating of optical fibres with thermally curable silicone resin using a pressurized die," Electron. Lett. **18**, 713 (1982).
[4] K. C. Chung and K. N. Astill, "Hydrodynamic instability of viscous flow between rotating coaxial cylinders with fully developed axial flow," J. Fluid Mech. **81**, 641 (1977).
[5] M. A. Hasoon and B. W. Martin, "The stability of viscous axial flow in an annulus with a rotating inner cylinder," Proc. R. Soc. London, Ser. A **352**, 351 (1977).
[6] D. I. Takeuchi and D. F. Jankowski, "A numerical and experimental investigation of the stability of spiral Poiseuille flow," J. Fluid Mech. **102**, 101 (1981).
[7] R. M. Lueptow, A. Docter, and K. Min, "Stability of axial flow in an annulus with a rotating inner cylinder," Phys. Fluids A **4**, 2446 (1992).
[8] A. Meseguer and F. Marques, "On the competition between centrifugal and shear instability in spiral Poiseuille flow," J. Fluid Mech. **455**, 129 (2002).
[9] D. L. Cotrell and A. J. Pearlstein, "The connection between centrifugal instability and Tollmien-Schlichting-like instability for spiral Poiseuille flow," J. Fluid Mech. **509**, 331 (2004).
[10] C. Canuto, M. Y. Hussaini, A. Quarteroni, and T. A. Zang, *Spectral Methods in Fluid Dynamics* (Springer, Berlin, 1988).

[11] A. Meseguer and F. Marques, "On the competition between centrifugal and shear instability in spiral Couette flow," J. Fluid Mech. **402**, 33 (2000).
[12] V. M. Sadeghi and B. G. Higgins, "Stability of sliding Couette-Poiseuille flow in an annulus subject to axisymmetric and asymmetric disturbances," Phys. Fluids A **3**, 2092 (1991).
[13] J. E. Mott and D. D. Joseph, "Stability of parallel flow between concentric cylinders," Phys. Fluids **11**, 2065 (1968).
[14] P. G. Drazin and W. H. Reid, *Hydrodynamic stability*, 2nd ed. (Cambridge University Press, Cambridge, England, 2004).